Applied Thermal Engineering 179 (2020) 115686

Contents lists available at ScienceDirect

Applied Thermal Engineering

journal homepage: www.elsevier.com/locate/apthermeng

Bioinspired heat exchangers based on triply periodic minimal surfaces for supercritical CO_2 cycles

Weihong Li[a,b,c,*], Guopeng Yu[a], Zhibin Yu[a]

[a] James Watt School of Engineering, University of Glasgow, UK
[b] Department of Mechanical and Aerospace Engineering, Hong Kong University of Science and Technology, Hong Kong, China
[c] HKUST Jockey Club Institute for Advanced Study, The Hong Kong University of Science and Technology, Clear Water Bay, Kowloon, Hong Kong, China

HIGHLIGHTS

- Triply Periodic Minimal Surface (TPMS) Structures were explored as heat exchanger in sCO2 cycle.
- TPMS structures generate much larger turbulent kinetic energy than printed printed circuit heat exchanger (PCHE).
- TPMS structures improve overall thermal performance by 15–100% compared with PCHE.

ARTICLE INFO

Keywords:
Supercritical carbon dioxide
Triply periodic minimal surface
Heat exchanger
Nusselt number
Conjugate heat transfer

ABSTRACT

The supercritical carbon dioxide (sCO_2) based Brayton cycle is a proposed alternative to replace conventional Rankine cycles in terms of high cycle efficiency, compact turbomachinery and heat exchangers. In the sCO_2 cycle, however, the existing heat exchangers have been challenged by large portion of heat transfer (approximately 60–70% of total cycle heat transfer) and high cycle efficiency required. In the present study, two novel heat exchangers were proposed by utilizing triply periodic minimal surface (TPMS) structures. i.e. the Gyroid structure and Schwarz-D surface, to enhance heat transfer and improve cycle efficiency. TPMS structures are a class of structures composed of two distinct inter-penetrating volume domains separated by an area-minimizing wall, which have been observed as biological membranes and co-polymer phases. Two heat exchangers along with a reference printed circuit heat exchanger (PCHE) were investigated numerically by computational fluid dynamics simulations when the hot and cold sCO_2 fluids pass through them at various Reynolds numbers. Effects of geometrical shapes and Reynolds number on the hydraulic and thermal performances were identified. It was demonstrated that two heat exchangers with TPMS can improve overall thermal performance by 15–100%, and the Nusselt number is raised by 16–120% for a given pumping power in comparison with the PCHE. Hence, heat exchangers with TPMS have a very good potential to enhance sCO_2 cycle efficiency.

1. Introduction

The supercritical CO_2 (sCO_2) Brayton cycle has the potential to replace steam Rankine cycles in electricity generation, due to its higher efficiency and compactness compared with steam Rankine cycles [1–4]. In the sCO_2 Brayton cycle, there are generally three types of heat exchangers, i.e., recuperators, pre-coolers, and heaters [5–7]. The heat exchanger effectiveness greatly affects the overall cycle efficiency of the sCO_2 Brayton cycle. Therefore, the development of heat exchangers with high efficiency gains a lot of attentions in the past decades. Traditional heat exchangers, like shell-and-tube heat exchanger [8], spiral wound heat exchangers [9], have been developed and applied into industries. However, problems still exist for theses heat exchangers such as large working space, high manufacturing cost, leakage and operational reliability and so forth. Recently proposed heat exchanger, namely printed circuit heat exchanger [10–13], has been a promising plate-type heat exchanger due to several advantages, including high heat transfer area density, endurance of pressure and temperature, and good compactness.

The heat transfer performance and pressure loss of PCHE in sCO2 cycle have been investigated experimentally and numerically, but in most of studies the conventional PCHE with continuous zigzag channel were focused. Ishizuka et al. [14] experimentally evaluated the thermal and hydraulic performance of a PCHE. Empirical correlations for local

* Corresponding author.
E-mail address: mewhli@ust.hk (W. Li).

https://doi.org/10.1016/j.applthermaleng.2020.115686
Received 12 February 2020; Received in revised form 9 June 2020; Accepted 30 June 2020
Available online 06 July 2020

Nomenclature

A	heat transfer area (m^2)
D_h	channel hydraulic diameter (mm)
f	friction factor
h_{local}	local heat transfer coefficient
HF	heat flux (W/m^2)
L_x	domain height (m)
L_y	domain spanwise length (mm)
L_z	domain streamwise length (mm)
m	mass flow rate (kg/s)
Nu	Nusselt number
P	pressure (Pa)
PEC	performance evaluation coefficient
Re	Reynolds number
Q	heat flux (W/m^2)
T	Temperature (K)
TKE	turbulent kinetic energy (m^2/s^2)
U	velocity (m/s)
WSS	wall shear stress magnitude (Pa)
x	coordinate (mm)
y	coordinate (mm)
z	coordinate (mm)

Greek symbols

λ	fluid thermal conductivity (W/(m·K))
μ	fluid dynamic viscosity (Pa·s)
ρ	density (kg/m^3)
τ_w	wall shear stress (Pa)
ω	vorticity (1/s)

Subscripts

b	bulk flow
c	cold channel
h	hot channel
in	inlet
k	Plane k
w	wall

heat transfer coefficient, overall heat transfer coefficient and frictional coefficient were developed based on their experimental data. They made one assumption that values of variables change linearly from inlet to outlet to deduce the local coefficients. Kwon et al. [15] numerically studied the heat transfer performance and pressure drop with respect to the angles of the zigzag-type PCHE. Water but not sCO_2 was used as the working fluid. Five types of zigzag channel with angles varying from 100 to 180° were designed and investigated. Optimal design for the zigzag-type PCHE has been reported based on the friction coefficients and Nusselt number. Nikitin et al. [16] experimentally studied the performance of the zigzag-type PCHE and compared with a two-dimensional numerical calculation. Correlations between the local heat-transfer coefficient and the pressure-drop factor were reported and suggested.

Besides conventional zigzag-type PCHE, previous studies have proposed to change the shapes of channel profile of the conventional zigzag-type PCHE for improved thermal and hydraulic performance. The main direction is to change the continuous channel type into discontinuous fin types, such as S-shape fin type (S-fin-type) and airfoil fin type. Tsuzuki et al. [17] proposed a PCHE with S-shape fins based on the pressure drop and heat transfer characteristics of PCHEs. It was concluded that the pressure drop of PCHE with S-shaped fins is one fifth of that with conventional zigzag PCHEs with identical heat transfer performance. Ngo et al. [18] experimentally studied the S-fin-type PCHE and the zigzag-type PCHE, compared their thermal–hydraulic performance, and proposed correlations of the Nusselt number and the pressure-drop factors. Their results showed that *Nu* of the zigzag-type PCHE was 25% to 35% higher and the pressure-drop factor was four to five times larger than those of the S-shaped fins. Kim et al. [19] proposed a PCHE with airfoil shaped fins and performed 3D simulations to study its thermal and hydraulic performance. The results were compared with the conventional zigzag PCHE. It was claimed that identical heat transfer performance could be achieved but at much lower pressure drop with airfoil shaped fins (one twentieth of pressure dropped in the zigzag fined PCHEs). Saeed et al. [20] proposed a new channel geometry for the PCHEs based on a staggered arrangement of sinusoidal fins. Simulations were performed using supercritical carbon dioxide (sCO2) as a working fluid. The sinusoidal fins were further optimized using response surface methodology in combination with the genetic algorithm. It was reported that the overall performance of the

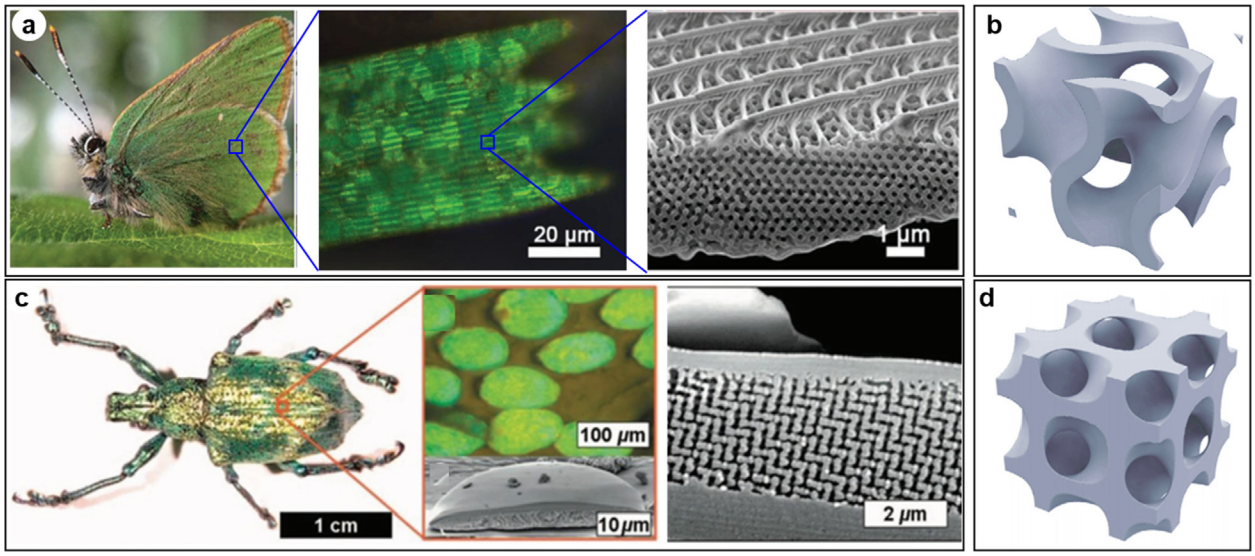

Fig. 1. (a) Photograph, high-magnifcation optical microscopic image, and SEM image of butterfly wing scales of species C. rubi. [23], (b) Computer-generated Gyroid cell model, (c) Photograph, high-magnifcation optical microscopic image, and SEM image of weevil L. augustus [24], (d) Computer-generated Schwarz-D cell model.

optimized proposed channel geometry was found up to 21% and 16% higher for the cold and hot side, respectively.

Completely new type of heat exchangers was also innovated to enhance the thermal and hydraulic performances. Pei et al. [21] proposed a honeycomb Ultra-compact Plate Heat Exchanger with hexagonal channels as recuperator in the SCO_2 Brayton cycle. They varied the geometry parameters and evaluate the performance via $Nu/f^{1/3}$. The results indicated that the UCPHE has a better overall performance than the Printed Circuit Heat Exchanger by about 15% within the investigated range of the Reynolds number. Jing et al. [22] introduced teardrop dimple and protrusions into the SCO_2 rectangular channels and obtained the detailed flow structures, friction and heat transfer characteristics, and overall thermal performance through numerical studies. The effects of geometrical structure, eccentricity of teardrop dimple/protrusion, Re, temperature and pressure of SCO_2 were investigated thoroughly. The results indicated that the overall thermal performance was enhanced by 17% compared with the smooth channel.

Based on the comprehensive review above, it is believed that most of studied on heat exchangers for sCO2 cycles are confined to PCHEs and just a few new forms of heat exchangers are proposed. In the present study, triply periodic minimal surface (TPMS) structures are applied to heat exchanger design to explore if there is the potential that the overall thermal performance of heat exchangers for sCO2 cycles can be enhanced significantly. Two heat exchangers with TPMS structures of the Gyroid and Schwarz-D types were designed, and the corresponding numerical simulations were launched to identify detailed flow fields, hydraulic loss and heat transfer characteristics, and overall thermal performance. The results were contrasted against a reference PCHE. It was identified that the heat exchangers with TPMS can enhance overall thermal performance by 15–100% compared with the PCHE, and for a given pumping power, the new exchangers can intensify Nusselt number by 16–120%.

2. Triply periodic minimal surfaces

Biological organisms have evolved complex and diverse hierarchical structures on the macro-, meso-, and micro-scales to realize different functions and adapt to natural environments. Triply periodic minimal surfaces and related materials have been widely found in biological systems like skeletons and scaffolds [23,24]. Fig. 1 shows two examples of TPMS topologies, i.e., Gyroid structure and Schwarz-D structure, discovered in the butterfly wing scales [23] and weevil Lamprocyphus augustus [24]. Fig. 1a shows optical microscopic image and scanning electron microscopy (SEM) images of the butterfly wing scales of species C. rubi [23]. The surface of the scales is covered by inter-connected ridges and ribs, providing mechanical stability of the scales and serving as interference reflectors. Note that the Gyroid structure is identified under the ribs, with a unit cell parameter of ≈300 nm. Fig. 1b shows that photonic crystal structures with Schwarz-D architectures in the scales of the weevil Lamprocyphus augustus [24]. It was reported that the unit cell parameter was around 450 nm. From a mathematical perspective, a surface that locally minimizes its area is referred as a minimal surface. For a certain boundary, a minimal surface is the surface with the least area that covers these boundaries. As a result, the minimal surface has smooth curvatures with no edges or corners. TPMS topologies with no self-intersections can partition space into two disjoint yet intertwining channels, which are simultaneously continuous [25]. The intertwining architectures have inherent properties and are lack of sharp edges with enhanced fluid dynamics. As the fluid dynamic principle suggests [26], a gradual enlargement or contraction of a flow path has substantially lower pressure drop than a sudden contraction or enlargement. The curved topology allows for smooth flow through the channels and is supposed to theoretically minimize the pressure drop. The interpenetrating structures of TPMS result in a favorable increase in turbulence causing improved heat and mass transfer [27]. The TPMS structures are known for their advanced mechanical properties [28] and anti-fouling capacity [29–31] due to topology local smoothness.

Level-set approximation technique [32] is utilized to obtain TPMS topologies. TPMS topologies have cubic symmetry and are repeated in the three-dimensional space. TPMS topologies split the space in two or more interconnected networks of volumes. Two possible ways can be employed to create structures [33]: the first is by thickening the surface to yield a sheet-based TPMS structure [33] and the second is by solidifying the volumes defined by the minimal surface to yield a skeletal based TPMS structure [34]. In the present study, we use two TPMS geometries, Gyroid structure and Schwarz-D structure, to generate TPMS structures, by thickening the surface to yield a sheet-based TPMS structure. These shapes are described by the following equations [35]:

$$\text{Gyroid:} \quad \cos(x)\sin(y) + \cos(y)\sin(z) + \cos(z)\sin(x) = 0 \tag{1}$$

$$\text{Schwarz} - \text{D:} \quad \cos(x)\cos(y)\cos(z) - \sin(x)\sin(y)\sin(z) = 0 \tag{2}$$

The surfaces facing towards the individual interweaving fluid channels are offset in two directions perpendicular to the surface, creating a solid surface wall with a homogeneous thickness for Gyroid and Schwarz-D structures.

3. Computational setup and validation

3.1. Computational domain and boundary conditions

In the present work, three different heat exchangers are investigated, i.e., PCHE, Gyroid structure, and Schwarz-D structure, which are shown in Fig. 2. The computational domains include two domains, one is solid domain, and the other is fluid domain that is composed of hot fluid channel and cold fluid channel. High temperature

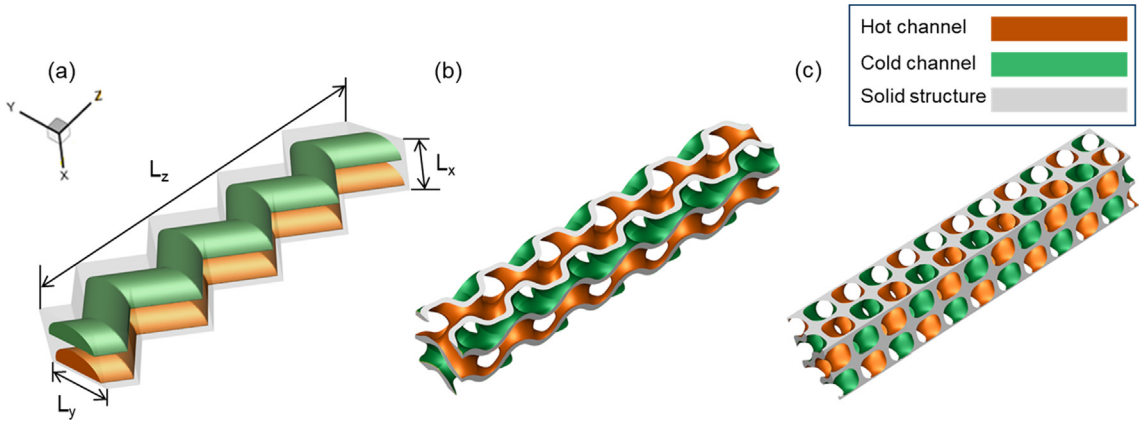

Fig. 2. Computational domain for (a) printed circuit heat exchanger (PCHE), (b) Gyroid structure, and (c) Schwarz-D structure.

Table 1
Geometrical parameters for three heat exchangers.

	PCHE	Gyroid	Schwarz-D
L_x [mm]	3.25	3.77	3.77
L_y [mm]	4.89	3.77	3.77
L_z [mm]	24	24	24
D_h [mm]	1.62	1.61	1.61
t [mm]	–	0.7	0.7
θ [°]	45	–	–

sCO_2 passes through the hot fluid channel, while the low temperature sCO_2 passes through the cold fluid channel in an opposite direction. Geometrical parameters are shown in Fig. 2, where L_x indicates height of the domains, L_y indicates spanwise length of the domains, and L_z is the streamwise length of the domains. Other detailed parameters are given in Table 1, where D_h is the hydraulic diameter of the fluid channel, t is the solid wall thickness, and θ is the turning angle of the zigzag channel of PCHE. The three structures have similar hydraulic diameter of fluid channels and streamwise length. The solid wall thickness of Gyroid and Schwarz-D structures is 0.7 mm, which is almost identical to the distance between hot channel and cold channel of PCHE.

Commercial software package ANSYS CFX 15.0 is used to solve the compressible and steady form of continuity, momentum and energy equations for the conjugate heat transfer process of sCO_2 heat exchanger. The shear stress transport (SST) turbulence model is used to simulate the turbulence effect, in which a dimensionless wall distance (y^+) less than 1.0 adopted. It has been shown that the SST turbulence model can provide much higher simulation accuracy than k-ε models [36]. The governing equations for the conjugate heat transfer process are provided by Eqs. (3)–(7).

Continuity equation:

$$\nabla \cdot \rho V = 0 \tag{3}$$

Momentum equation:

$$\rho(V \cdot \nabla V) = -\nabla p + \nabla \cdot \tau \tag{4}$$

where τ is stress tensor that is given by Eq. (5)

$$\begin{aligned} \tau &= (\mu + \mu_t)\left(\nabla V + (\nabla V)^T - \tfrac{2}{3}\delta \nabla \cdot V\right) \\ &= \mu\left(\nabla V + (\nabla V)^T - \tfrac{2}{3}\delta \nabla \cdot V\right) + \nabla \cdot \prod \end{aligned} \tag{5}$$

where Π is Reynolds stress tensor.

Energy equation:

$$\nabla \cdot (\rho V H) = \nabla \cdot \left(\frac{\lambda + \lambda_t}{c_p} \nabla h\right) \quad \text{(For fluid domain)} \tag{6}$$

$$k_s \nabla^2 T = 0 \quad \text{(For solid domain)} \tag{7}$$

To enhance the simulation robustness and accuracy, temperature and pressure boundary conditions are chosen for fluid inlets whereas mass flow rate is imposed at fluid outlets. Table 2 shows the boundary conditions for inlets and outlets. The temperature and pressure are fixed for both hot channel and cold channel. However, the mass flow rate is varied to achieve a range of Reynolds number of hot channel Re_h from 2300 to 53,000 and cold channel Re_c from 3000 to 70,000, respectively. Periodic boundary condition is applied to the top, bottom, and both sides of the domains. Coupled boundary condition is imposed to the fluid–solid interfaces.

Since the geometries of the gyroid and schwarz-D structures are

Table 3
Comparison of present results and experimental results [14].

	Present	Literature	% Difference
Pressure drop, hot side [Pa]	25,065	24,180	3.66%
Pressure drop, cold side [Pa]	75,599	73,220	3.25%
Temperature difference, hot side [K]	173.08	169.6	2.05%
Temperature difference, cold side [K]	143.92	140.38	2.52%

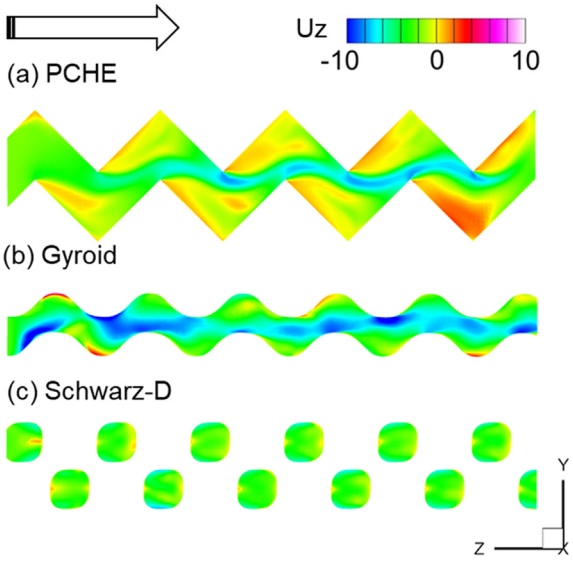

Fig. 3. Streamwise velocity distribution on the center plane of cold channel at Re_c = 15,300.

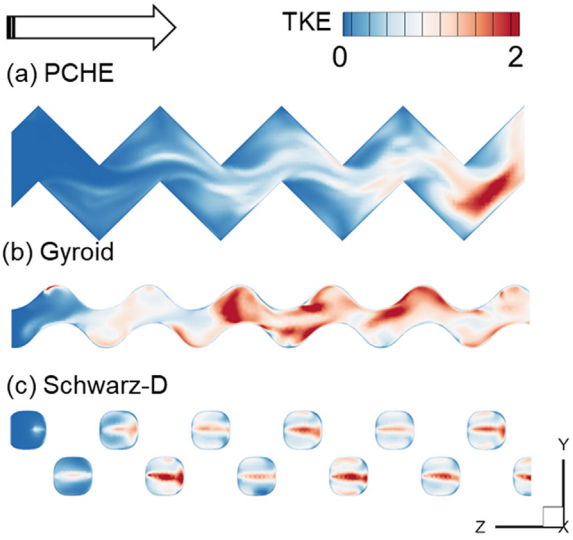

Fig. 4. Turbulent kinetic energy (TKE) distribution on the center plane of cold channel at Re_c = 15,300.

Table 2
Boundary conditions at inlets and outlets of fluid channel.

Hot side			Cold side		
P_{hi} [KPa]	T_{hi} [K]	m_h [kg s^{-1}]	P_{ci} [KPa]	T_{ci} [K]	m_c [kg s^{-1}]
2545.5	553	2.488e−4 ~ 5.723e−3	8283.81	494	3.281e−4 ~ 7.844e−3

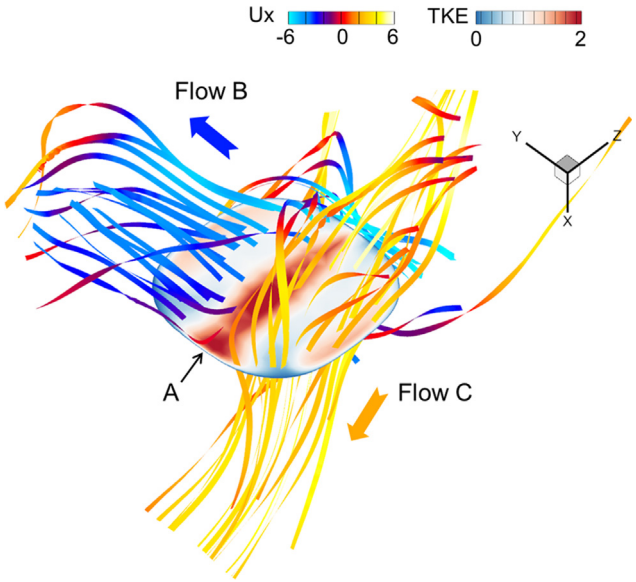

Fig. 5. High TKE region in Schwarz-D channel.

complex, unstructured meshes consisting of tetrahedron and prism elements are generated in ANSYS ICEM. A fine mesh with eleven layers of prism elements is generated near the wall, and the thickness of the first layer element is set as ~0.00025 mm to guarantee the y^+ value around 1. For regions away from walls and solid domain, relatively coarse meshes are produced to save computational time and cost. The total elements of the mesh are set around 7 million after mesh independence study. Smooth transition between different regions is ensured to minimize numerical errors. Conformal interfaces are adopted to couple the fluid domains and solid domain for accurate data transfer.

3.2. Properties of CO_2

Supercritical fluids show significant variations in the thermophysical properties near the critical point, which substantially influence the thermal–hydraulic performances of heat exchangers. Therefore, it is imperative to consider the variations when simulating heat exchangers with CO_2 as a working fluid. In the present work, fluid properties table written in a specific format (RGP file) is implemented into ANSYS CFX to interpolate fluid properties during numerical iterations. The fluid properties table includes necessary properties with temperatures and pressures ranging from 300 K, 1 MPa to 1100 K, 20 MPa. The accuracy of CFX interpolation using RGP table has been validated against the REFPROP in previous work [36].

3.3. Computational model validation

To validate the computational model, a PCHE that has similar geometries to Ishizuka et al. [14] and Kim et al. [19] is used, which has dimensions of 4.89 (L_x) × 7.74 (L_y) × 846 (L_z) mm. Fine meshes are generated for the new PCHE geometry using above-mentioned mesh generation methods. Table 3 shows the comparison of present numerical results with previous validated numerical results [14]. The difference falls within 3.7%, which indicates the high prediction accuracy of the present simulation method. Therefore, the present numerical method and turbulence model are capable to provide accurate data for flow field and heat transfer analysis.

4. Results and discussions

In the present work, thermal and hydraulic performances are evaluated through two parameters: Nusselt number (*Nu*) and friction factor (*f*). The *Nu* number is calculated based on local heat transfer coefficient h_{local}, hydraulic diameter, and fluid thermal conductivity. The local heat transfer coefficient h_{local} is obtained as Eq. (8) [36]. Local *Nu* number and average *Nu* number obtained by integrating over the whole channel are expressed as Eq. (9) [36].

$$h_{local} = \frac{Q/A}{T_{wall} - T_{bulk}} \tag{8}$$

where h_{local}, Q, A, T_{wall}, and T_{bulk} are local heat transfer coefficient, heat flux through the wall, heat transfer area, wall temperature, and bulk flow average temperature, respectively.

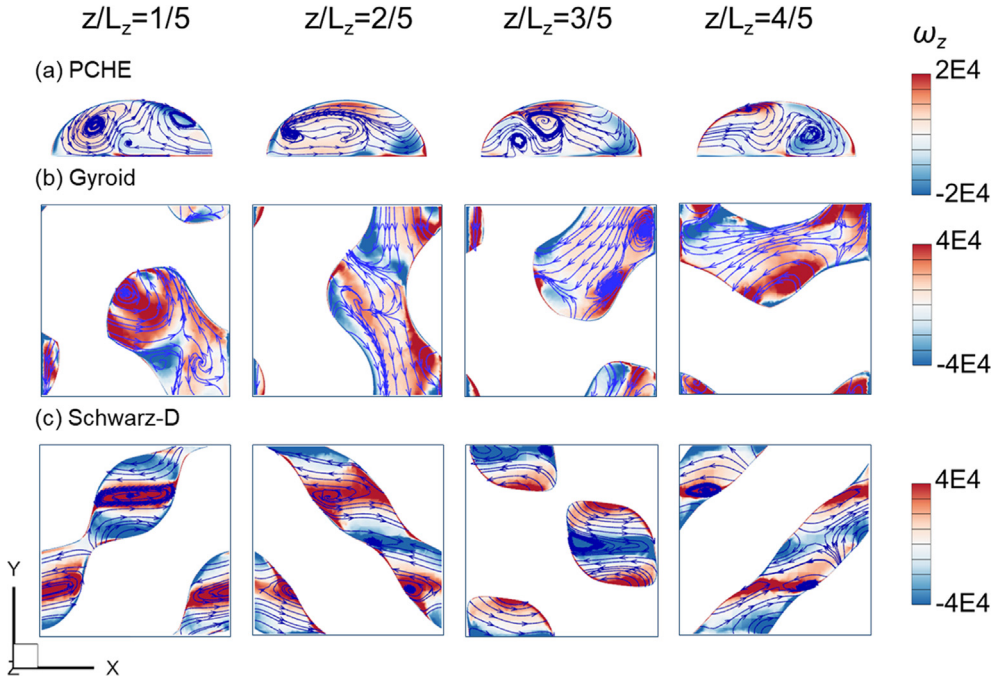

Fig. 6. Streamwise vorticity and streamlines on the four planes of cold channel, Re_c = 52,000.

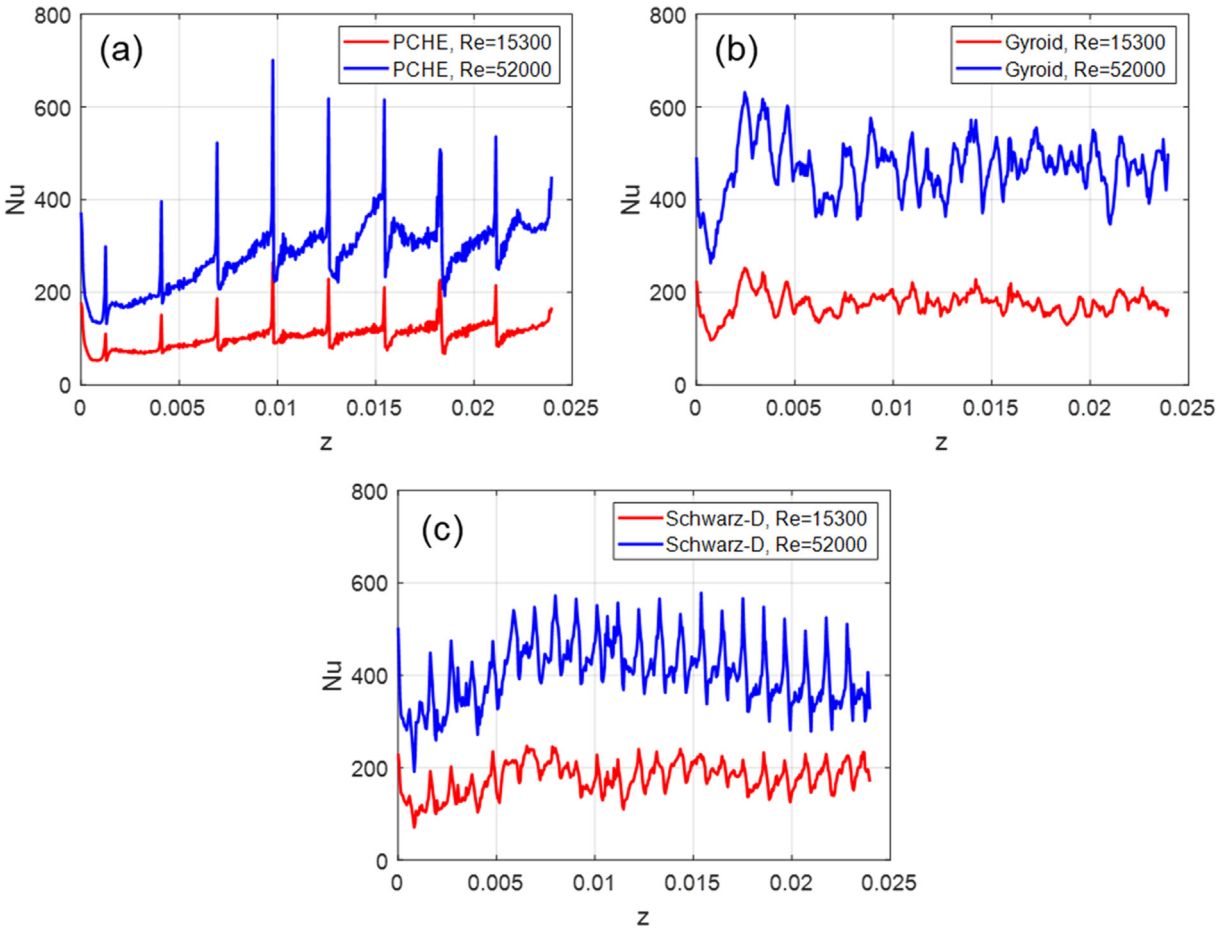

Fig. 7. Spanwise-averaged *Nu* number of cold channel with varying *Re* numbers.

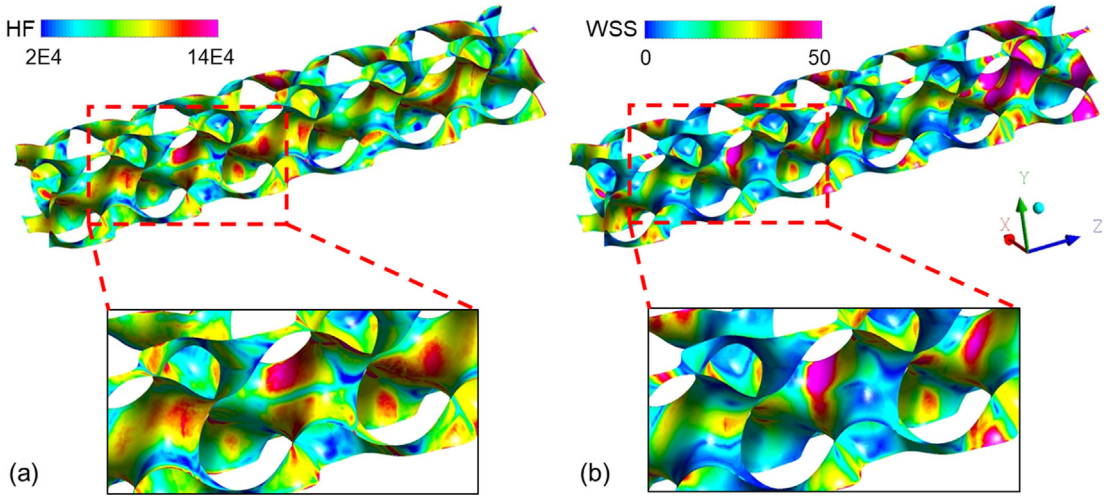

Fig. 8. (a) Heat flux and (b) wall shear stress magnitude distributions of the cold channel of Gyroid at $Re = 15{,}300$.

$$Nu = \frac{h_{local} D_h}{k_f}, \quad \bar{Nu} = \frac{1}{n}\sum_{i=1}^{k} Nu_i \tag{9}$$

where D_h and k_f are hydraulic diameter of fluid channel and fluid thermal conductivity, respectively. Local friction factor is calculated using a number of plane-averaged pressures in the streamwise direction. The local friction factor and averaged friction factor are calculated by Eq. (10) [36].

$$f = \frac{(P_{in} - P_k)}{2\rho_k V_k^2}\left(\frac{D_h}{L_k}\right), \quad \bar{f} = \frac{1}{n}\sum_{i=1}^{k} f_i \tag{10}$$

Here, P_{in}, P_k, ρ_k, V_k, and L_k are the plane-averaged pressure at channel inlet, plane-averaged pressure at plane k, plane-averaged velocity at plane k, and length from inlet to plane k, respectively. The overall thermal performance is evaluated through a variable called performance evaluation coefficient (PEC), which is defined as Eq. (11) [36].

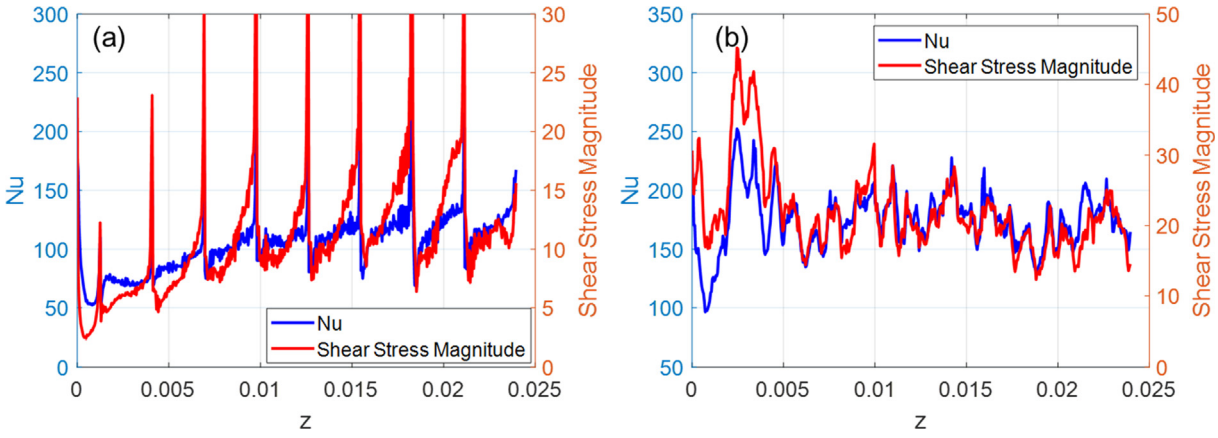

Fig. 9. Spanwise averaged *Nu* number and shear stress magnitude for (a) PCHE and (b) Gyroid.

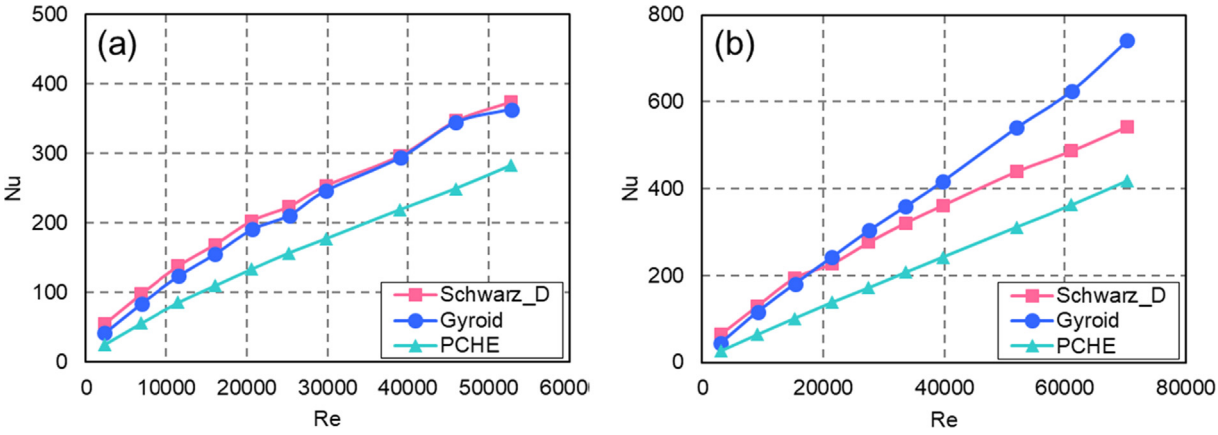

Fig. 10. Area averaged *Nu* number of (a) hot channel and (b) cold channel.

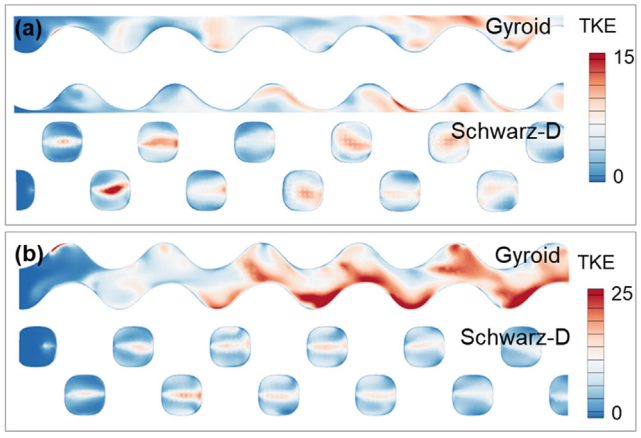

Fig. 11. Turbulent kinetic energy (TKE) distribution on the center plane of (a) hot channel at Re_h = 39000, and (b) cold channel at Re_c = 52000.

$$PEC = \frac{Nu/Nu_{PCHE}}{\sqrt[3]{f/f_{PCHE}}} \tag{11}$$

4.1. Fluid flow characteristics

In this section, the bulk flow field and turbulence features of different heat exchangers will be analysed. Mean flow field, turbulent kinetic energy, and vorticity will be extracted and compared to show how geometry variations can affect the flow dynamics and turbulence transportation.

The distributions of streamwise velocity U_z on the center plane of cold channel at Re_c = 15300 are shown in Fig. 3. The black arrow denotes the flow direction in the cold channel. In Fig. 3a, periodic flow circulation regions are induced by the zigzag turnings, and the recirculation region grows larger with the increase of streamwise distance, even occupies half of the channel at the final turning. The middle plane of the Gyroid structure resembles the sinusoidal fin geometry [20], as shown in Fig. 3b. Less severe recirculation is observed in the turning regions. However, discrete spots with large streamwise velocity are observed, which is suspected to be caused by complex interconnecting fluid channels. Fig. 3c shows the uniform velocity distribution without obvious flow recirculation in Schwarz-D structure, which is unfavorable for turbulence production.

Fig. 4 shows the corresponding turbulent kinetic energy (TKE) distribution on the center plane of cold channel at Re_c = 15,300. It is observed in Fig. 4a that, even though with severe recirculation behind turnings, the turbulent kinetic energy is relatively low compared with Gyroid and Schwarz-D structures. This might be ascribed to the less intrinsically complex channel shape than the Gyroid and Schwarz-D structures. Fig. 4b shows that the Gyroid produces the highest TKE due to strong flow mixing in interconnected channel. The strong turbulence mixing is supposed to be favorable for heat transfer enhancement whereas increases pressure losses across the channel, which may finally degrade the thermal–hydraulic performance. For the Schwarz-D structure, Fig. 4c shows an overall lower TKE level than the Gyroid structure but exhibits high TKE regions in the center of channel, which is caused by unique flow patterns inside the Schwarz-D channels shown in Fig. 5.

The complicated flow patterns inside the Schwarz-D channel is shown in Fig. 5. The contour shows the TKE distribution on the middle plane similar to Fig. 4c. Two clusters of streamlines with opposite flow

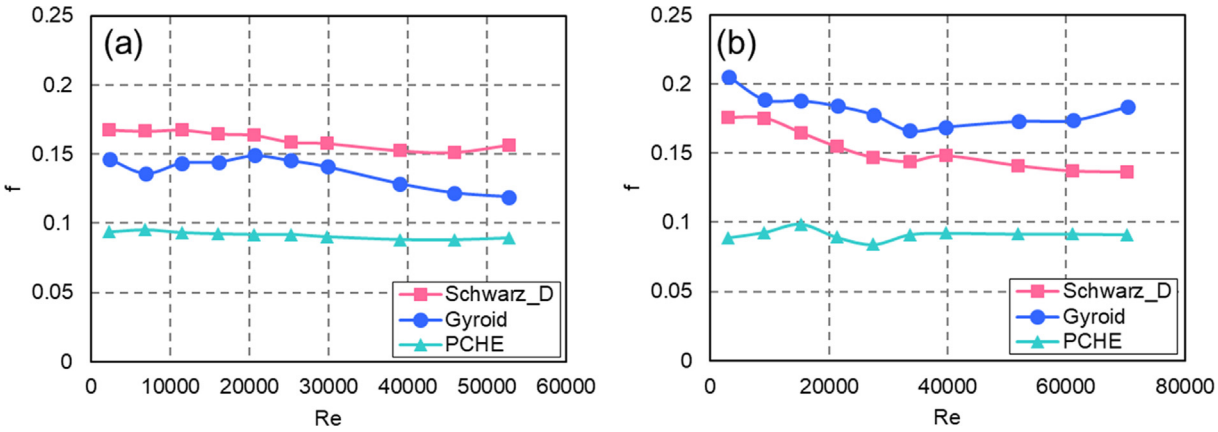

Fig. 12. Area averaged friction factor for (a) hot channel and (b) cold channel.

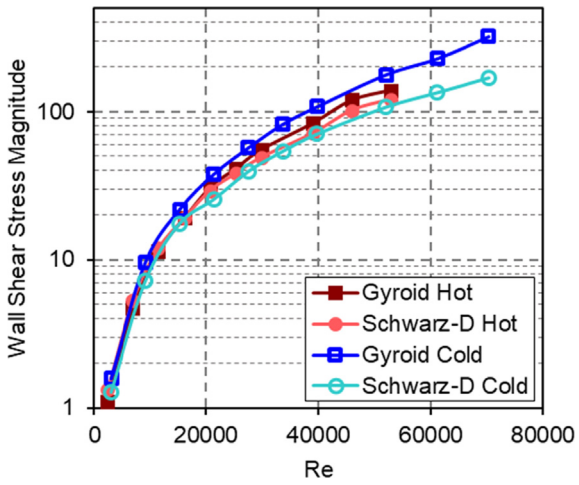

Fig. 13. Area averaged wall shear stress magnitude for hot and cold channels.

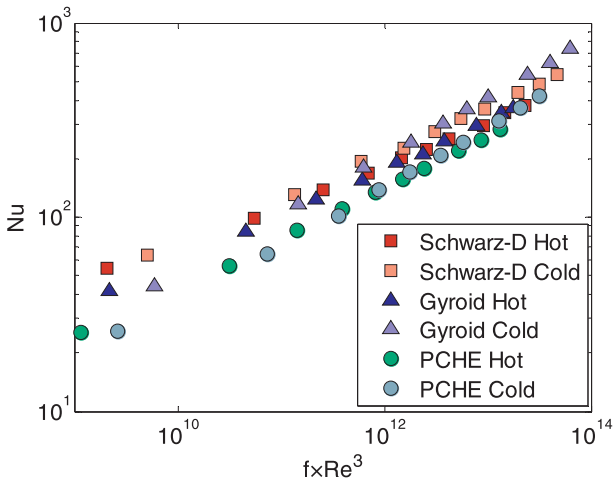

Fig. 15. Comparison of overall thermal performance for three heat exchangers.

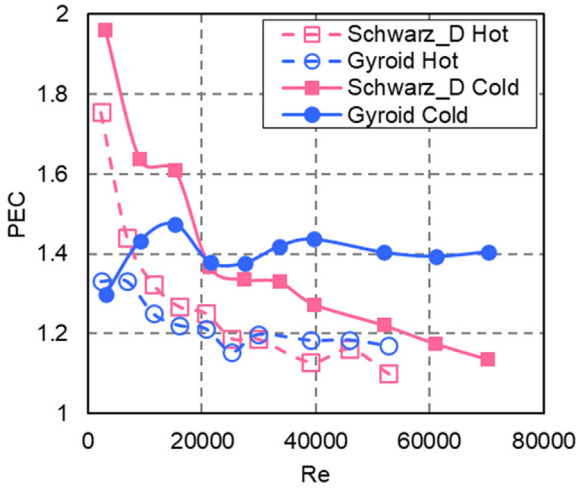

Fig. 14. Area averaged thermal performance evaluation coefficient (PEC) for hot and cold channels.

directions are apparently observed and denoted with flow B and flow C. The complex interconnected channels result in two streams of flows passing through one channel simultaneously. In particular, flow B has negative U_x while flow C has positive U_x, which leads to strong shearing effect and large velocity gradient in region A. The large shearing in region A causes significant turbulent production and large turbulent kinetic energy.

A detailed illustration of streamwise vorticity and streamlines on the four planes of cold channel is shown in Fig. 6. The four planes correspond to streamwise locations from z/L_z = 1/5 to 4/5. The figure shows the vortex evolutions along the streamwise direction for three heat exchangers, along with the streamwise vorticity ω_z. Generally, the streamwise vorticity levels of Gyroid and Schwarz-D structures are higher than these of PCHE. This is due to more complex channel orientations that produce significant velocity gradient and thus the streamwise vorticity ω_z. Fig. 6a shows that there are two main counter rotating vortices in the PCHE channel, and the spanwise shift of vortices along the streamwise locations are mainly caused by varying bend orientations. In the Gyroid channel, vortices distribute more randomly, and small portions of the vortices have similar sizes to the channel size. However, in the Schwarz-D channel, vortices have more organized profile. In particular, the negative and positive vorticity regions distribute alternatively and periodically in y direction. Also note that large portions of these vortices have similar sizes to the channel size. Generally, the vortex revolutions along the streamwise locations for Gyroid and Schwarz-D structures exhibit more substantial complexity than PCHE, which results in higher thermal performance as explained in the next section.

4.2. Heat transfer characteristics

In this section, the local heat transfer characteristics will be shown, and the underlying fluid mechanisms will be provided. The local heat transfer characteristics include temperature and heat flux contour distributions and spanwise averaged *Nu* number along the streamwise

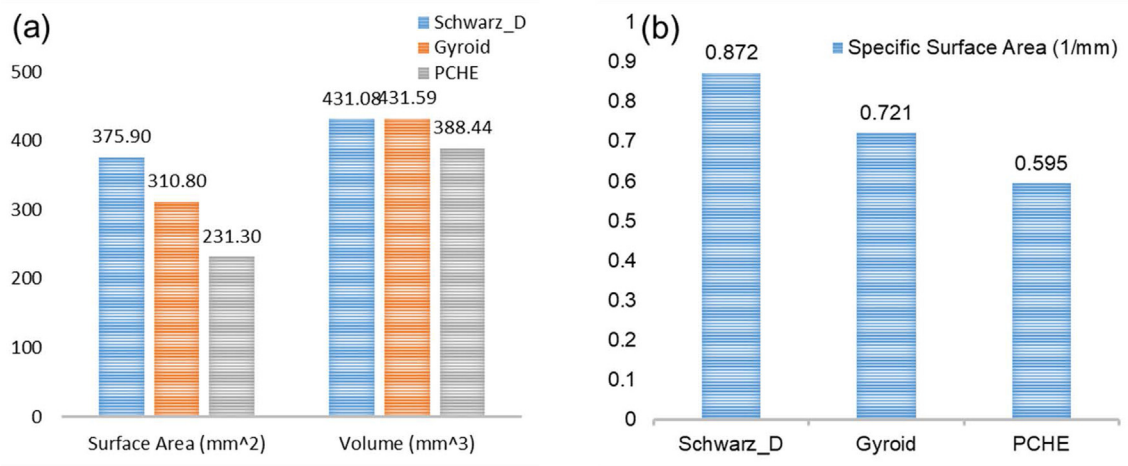

Fig. 16. (a) Surface area and volume and (b) Specific heat transfer area.

direction. Fig. 7 shows the spanwise-averaged *Nu* number of cold channel with varying *Re* numbers. The spanwise averaged *Nu* number is obtained by averaging the *Nu* number along the streamwise direction. For PCHE, Fig. 7a shows that the *Nu* number distributes periodically and gradually increases with the increase of streamwise locations. Significant peak values are observed at the bending regions which are caused by high velocity gradient and turbulence mixing. These peak values are also reported by Saeed et al. [36]. Fig. 7b and c shows that the Gyroid and Schwarz-D structures produce more frequent fluctuating distributions of *Nu* number and have higher heat transfer level than PCHE. It is also observed that the Gyroid and Schwarz-D structures produce approximately similar heat transfer rates.

The underlying fluid mechanisms for the local heat transfer characteristics of the Gyroid structure is explained by relating the wall heat flux (HF) with the wall shear stress magnitude (WSS) contour distributions, which are shown in Fig. 8. Fig. 8a shows the wall heat flux distribution with an enlarged view. One can observe discrete regions with high heat flux at the junction regions, since the cold flow is blocked by these junctions, which forms an impingement effect and breaks the boundary layer. Then, new boundary layer forms and the heat flux is substantially enhanced. Fig. 8b shows that regions with high heat flux and wall shear stress magnitude almost coincide. This phenomenon can be explained by Reynolds analogy, which is expressed by Eq. (12) [37].

$$\dot{q}_w \approx \frac{\tau_w c_p (T_w - T_\infty)}{V_\infty} \tag{12}$$

Here, τ_w, c_p, T_∞, and V_∞ are wall shear stress, specific heat capacity, mainstream temperature, and mainstream velocity. The Reynolds Analogy is to relate turbulent momentum and heat transfer, since the transport of momentum and the transport of heat largely depends on the same turbulent eddies. From Eq. (12), it is seen that the wall heat flux is proportional to wall shear stress. Therefore, regions with high wall shear stress usually correspond to regions with high heat flux.

The spanwise averaged *Nu* number and shear stress magnitude for PCHE and Gyroid structure are shown in Fig. 9. It quantitatively demonstrates that the spanwise averaged shear stress magnitude and Nusselt number have similar trends. In particular, the peak and valley values of *Nu* number almost coincide these of shear stress magnitude. It is also observed that the Gyroid structure shows overall higher shear stress magnitude than the PCHE, which is the underlying fluid mechanism for higher *Nu* number for Gyroid structure. It is anticipated that the Schwarz-D structure will also have high level of shear stress magnitude. One advantage of the high shear stress of Gyroid is that it may indicate higher and favorable anti-fouling capacity. However, differences between spanwise averaged shear stress magnitude and Nusselt number can also be observed, which is suspected to arise in areas of recirculation, since the flow can experience an adverse pressure gradient, while there is no analogous mechanism for heat transfer.

4.3. Overall pressure drop and thermal performance

At a given Reynolds number, the Gyroid and Schwarz-D structures provides superior heat transfer than the PCHE due to higher turbulent kinetic energy production. Meanwhile, higher turbulent kinetic energy will lead to higher pressure drop. Therefore, it is beneficial to characterize the overall thermal performance of these heat exchangers.

Fig. 10 shows the area averaged *Nu* number of both hot and cold channels for three heat exchangers. It is observed that the *Nu* number increases with the increase of Reynolds number for the three structures. In Fig. 10a, the Gyroid and Schwarz-D structures have almost similar *Nu* number trend for the whole range of *Re* numbers investigated, which is suspected to be caused by quite identical level of turbulent kinetic energy of the two structures, as shown in Fig. 11a. Also note that Gyroid and Schwarz-D structures show higher heat transfer level than PCHE by 30–65%. The heat transfer enhancement is ascribed to more significant production of turbulent kinetic energy in Gyroid and Schwarz-D structures. For the cold channel in Fig. 10b, the advantage of Gyroid structure over Schwarz-D structure grows stronger as Reynolds number becomes higher, which can be explained from Fig. 11b that Gyroid produces much higher turbulence production than Schwarz-D at high *Re* number. Additionally, the Gyroid and Schwarz-D structures produce higher *Nu* number than PCHE by averagely 80% and 65%, respectively.

Friction factor is another imperative aspect for evaluating the overall thermal performance, which is defined in Eq. (10). Fig. 12 shows the averaged friction factor for both hot and cold channels. Overall, Gyroid and Schwarz-D structures produce higher friction factors than PCHE by 50–100%, which are caused by stronger turbulence mixing and much higher wall shear stresses. In particular, Schwarz-D structure produces higher friction factor than Gyroid structure in hot channel, while the trend is reversed in cold channel. This is caused by synergetic effects of wall shear stress and the shear stress between the fluid flows within. A portion of the friction loss results from wall shear stress between the surfaces and fluids, as shown in Fig. 13. The other portion is determined from the shearing and mixing of fluid flows within, which is related to the velocity gradient and is indirectly reflected by turbulent kinetic energy. For the hot channel, it is shown that the wall shear stress for Gyroid and Schwarz-D structures are comparable. It is also found in Fig. 11a that the Gyroid structure has quite identical level of turbulent kinetic energy with the Schwarz-D structure, which represents that the friction losses from fluid within the bulk flows are comparable for the two structures. However, the Schwarz-D

structure has higher surface area, and so the total pressure drop and friction factor are higher. For the cold channel, Figs. 4 and 11b exhibit that the turbulent kinetic energy of the Gyroid structure is substantially higher than that of the Schwarz-D structure. Moreover, the difference of wall shear stress between the Gyroid structure and the Schwarz-D structure grows larger with the increase of Reynolds number. Therefore, the Gyroid structure produces higher turbulent kinetic energy and thus shear stress within the fluid, as well as wall shear stress, which result in higher friction factor than the Schwarz-D structure.

The overall thermal performance is evaluated using the performance evaluation coefficient (PEC), which is defined as Eq. (11). The coefficient uses the thermal performance and pressure drop of PCHE as base values. Fig. 14 plots the PEC values of Gyroid and Schwarz-D structures for both hot and cold channels. Generally, the Gyroid and Schwarz-D structures outperform the PCHE by 17–100%, with higher superiority at lower Reynolds number. For the hot channel, Schwarz-D structure produces higher PEC values than Gyroid when *Re* is lower than 30000, while has lower PEC values when *Re* is higher than 30,000. For the cold channel, the same tendency holds but the turning *Re* number is 20,000. The complex trend is the result of combined effects of enhanced surface area and increased turbulence production. When *Re* number is low, the turbulent kinetic energy is comparable for the two structures, so the heat transfer surface area determines the PEC values. The Schwarz-D structure has higher heat transfer surface area, resulting in higher heat transfer rate. However, for higher *Re* number, the turbulence production in Gyroid is increased dramatically and turbulence mixing plays a dominant role in enhancing heat transfer level. Therefore, the Gyroid structure shows higher PEC values than the Gyroid structure. The thermal and hydraulic mechanism applies to both hot and cold channels, but certain difference exists when it determines the turning *Re* number.

In real sCO_2 cycle conditions, the pumping powers of the compressor are usually fixed, and it is desirable to achieve higher heat transfer performance for a given pumping power. Therefore, it is beneficial to characterize the heat transfer performance as a function of pumping power. The pumping power is proportional to $f_H Re_H^3$ [38]. Fig. 15 exhibits the comparison of overall thermal performance for three heat exchangers. For a given pumping power, the Schwarz-D cold channel generally provides higher *Nu* number than the Schwarz-D hot channel, reaching 35% at the high values of $f_H Re_H^3$. However, for Gyroid structure and PCHE, hot channels provide higher *Nu* number for a low pumping power, while cold channels show better heat transfer performance for a high pumping power. For the hot channel, the Gyroid and Schwarz-D structures show higher *Nu* number by 85% and 16% at a low and high pumping power, respectively. For cold channel, the *Nu* number of the Gyroid and Schwarz-D structures are higher than PCHE by around 40–120% for a given pumping power.

The advantage of triply periodic minimal surface structures not only lies in complex interconnect channels that prompt turbulence mixing, but also increase surface area for heat transfer area that further enhance heat transfer efficiency. Fig. 16 shows the surface area, volume, and specific heat transfer area for three structures. In Fig. 16a, it is seen that the Schwarz-D structure has the highest heat transfer surface area, while the PCHE has the lowest. The volume of Gyroid and Schwarz-D structures are similar, while the PCHE shows slightly lower value. Hence, it is necessary to consider specific heat transfer area. Fig. 16b shows the specific heat transfer area of the three structures. It is obvious that the Schwarz-D structure has the highest specific heat transfer area, about 21% and 47% higher than Gyroid and PCHE, respectively.

5. Conclusions

In the present work, a novel heat exchanger based on triply periodic minimal surface structures was proposed and studied through computational fluid dynamic simulations. The flow structures and heat transfer characteristics are obtained to evaluate its potential application in supercritical CO_2 Brayton cycle.

The TPMS and PCHE produce different flow structures. In the PCHE, large separations occur while the turbulent kinetic energy is the lowest. For TPMS structures, only small separations are generated in Gyroid and Schwarz-D due to smooth topology. However, large turbulent kinetic energy production is observed in Gyroid structure, which is suspected to be caused by complex flow mixing and is favourable for heat transfer enhancement. Moreover, there exist regions with large turbulent kinetic energy appear in the channel centre of Schwarz-D structure, which is caused by significant shearing due to opposite flow directions in one channel.

The TPMS structures show much higher heat transfer rate than the PCHE. Compared with PCHE, heat transfer enhancement by 30–80% is achieved with Gyroid and Schwarz-D structures, while friction loss is elevated by 50–100%. Considering overall thermal performance, Gyroid and Schwarz-D structures outperform the PCHE by 15–100%, due to enhanced surface area and increased turbulence production. For a given pumping power, the Gyroid and Schwarz-D structures produce higher heat transfer coefficient than PCHE by 16–120%.

The results of the investigation are helpful to understand the flow dynamics and heat transfer performance in TPMS structures, which is of great significance for the development and optimization of advanced heat exchangers. More TPMS structures are worth of further investigations. In addition, optimization studies concerning with dividing wall thickness or void fraction can be performed to achieve better thermal performance in future studies. The present studies are believed to provide important reference data for practical engineering applications.

Declaration of Competing Interest

The authors declare that they have no known competing financial interests or personal relationships that could have appeared to influence the work reported in this paper.

Acknowledgments

The work benefited from the financial support by EPSRC in the UK (EP/N020472/1, EP/N005228/1, EP/P028829/1 and EP/R003122/1).

References

[1] Y.u. Yang, W. Bai, Y. Wang, et al., Coupled simulation of the combustion and fluid heating of a 300MW supercritical CO2 boiler, Appl. Therm. Eng. 113 (2017) 159–267.
[2] F. Crespi, G. Gavagnin, D. Sánchez, G.S. Martínez, Supercritical carbon dioxide cycles for power generation: a review, Appl. Energy 195 (2017) 152–283.
[3] R. Singh, S.A. Miller, A.S. Rowlands, P.A. Jacobs, Dynamic characteristics of a direct-heated supercritical carbon-dioxide Brayton cycle in a solar thermal power plant, Energy 50 (2013) 194–204.
[4] A. Moisseytsev, J.J. Sienicki, Investigation of alternative layouts for the supercritical carbon dioxide Brayton cycle for a sodium-cooled fast reactor, Nucl. Eng. Des. 239 (2009) 1362–1371.
[5] T. Conboy, S. Wright, J. Pasch, D. Fleming, G. Rochau, R. Fuller, Performance characteristics of an operating supercritical CO2 Brayton cycle, J. Eng. Gas Turbines Power 134 (2012) 111703.
[6] W.-X. Chu, X.-H. Li, T. Ma, et al., Experimental investigation on SCO2-water heat transfer characteristics in a printed circuit heat exchanger with straight channels, Int. J. Heat Mass Transf. 113 (2017) 184–194.
[7] J. Sarkar, Second law analysis of supercritical CO2 recompression Brayton cycle, Energy 34 (2009) 1172–1178.
[8] L.G. Hackemesser, L.E. Cizmar, R.S. Burlingame, Shell and tube heat exchanger with impingement distributor, Appl. Therm. Eng. 18 (6) (1997) XIII.
[9] Z. Zhang, J. Xue, Y. Wang, Y. Li, Research and development of LNG wound-tube heat exchanger, China Petrol. Mach. (2015).
[10] D. Southall, S.J. Dewson, Innovative compact heat exchangers, Group 226 (2010) 583.
[11] Z.H. Ayub, Plate heat exchanger literature survey and new heat transfer and pressure drop correlations for refrigerant evaporators, Heat Transfer Eng. 24 (2003) 3–16.
[12] B.O. Neeraas, A.O. Fredheim, B. Aunan, Experimental data and model for heat transfer, in liquid falling film flow on shell-side, for spiral-wound LNG heat

exchanger, Int. J. Heat Mass Transfer 47 (2004) 3565–3572.
[13] J.S. Jayakumar, S.M. Mahajani, J.C. Mandal, P.K. Vijayan, R. Bhoi, Experimental and CFD estimation of heat transfer in helically coiled heat exchangers, Chem. Eng. Res. Des. 86 (2008) 221–232.
[14] T. Ishizuka, Y. Kato, Y. Muto, K. Nikitin, N.L. Tri, H. Hashimoto, Thermal–hydraulic characteristic of a printed circuit heat exchanger in a supercritical CO2 loop, The 11th International Topical Meeting on Nuclear Reactor Thermal–Hydraulics (NURETH-11), (2005).
[15] O.K. Kwon, M.J. Choi, Y.J. Choi, Heat transfer and pressure drop characteristics in zigzag channel angles of printed circuit heat exchangers, Korean J. Air Cond. Refrig. Eng. 21 (9) (2009) 475–482.
[16] K. Nikitin, Y. Kato, T.L. Ngo, Printed circuit heat exchanger thermal–hydraulic performance in supercritical CO2 experimental loop, Internat. J. Refrig. 29 (2006) 807–814.
[17] N. Tsuzuki, Y. Kato, T. Ishiduka, High performance printed circuit heat exchanger, Appl. Therm. Eng. 27 (10) (2007) 1702–1707.
[18] T.L. Ngo, Y. Kato, K. Nikitin, N. Tsuzuki, New printed circuit heat exchanger with Sshaped fins for hot water supplier, Exp. Therm. Fluid Sci. 30 (8) (2006) 811–819.
[19] D.E. Kim, M.H. Kim, J.E. Cha, S.O. Kim, Numerical investigation on thermal-hydraulic performance of new printed circuit heat exchanger model, Nucl. Eng. Des. 238 (12) (2008) 3269–3276.
[20] M. Saeed, M.-H. Kim, Thermal-hydraulic analysis of sinusoidal fin-based printed circuit heat exchangers for supercritical CO2 Brayton cycle, Energy Convers. Manage. 193 (2019) 124–139.
[21] B. Pei, Z. Chen, F. Li, B. Bai, Flow and heat transfer of supercritical CO2 in the honeycomb ultra-compact plate heat exchanger, J. Supercrit. Fluid 148 (2019) 1–8.
[22] Q. Jing, Y. Xie, D. Zhang, Thermal-hydraulic performance and entropy generation of supercritical carbon dioxide in heat exchanger channels with teardrop dimple/protrusion, Int. J. Heat Mass Transf. 113 (135) (2019) 1082–1096.
[23] R.W. Corkery, E.C. Tyrode, On the colour of wing scales in butterflies: iridescence and preferred orientation of single gyroid photonic crystals, Interface focus 7 (4) (2017) 20160154.
[24] J.W. Galusha, L.R. Richey, J.S. Gardner, J.N. Cha, M.H. Bartl, Discovery of a diamond-based photonic crystal structure in beetle scales, Phys. Rev. E 77 (5) (2008) 050904.
[25] S. Torquato, A. Donev, Minimal surfaces and multifunctionality, Philos. Trans. R. Soc. A Math. Phys. Eng. Sci. 460 (2004) 1849–1856.
[26] B.R. Munson, T.H. Okiishi, W.W. Huebsch, A.P. Rothmayer, Fundamentals of fluid mechanics, J. Mech. Work. Technol. (2013) 1–196.
[27] E.A. Lord, A.L. Mackay, Periodic minimal surfaces of cubic symmetry, Curr. Sci. 85 (2003) 346–362.
[28] S.C. Kapfer, S.T. Hyde, K. Mecke, C.H. Arns, G.E. Schröder-Turk, Minimal surface scaffold designs for tissue engineering, Biomaterials (2011) 1–5.
[29] P.Z. Culfaz, S. Buetehorn, L. Utiu, M. Kueppers, B. Bluemich, T. Melin, M. Wessling, R.G.H. Lammertink, Fouling behavior of microstructured hollow fiber membranes in dead-end filtrations: critical flux determination and NMR imaging of particle deposition, Langmuir 27 (5) (2011) 1643–1652.
[30] P.Z. Culfaz, M. Wessling, R.G.H. Lammertink, Fouling behavior of microstructured hollow fiber membranes in submerged and aerated filtrations, Water Res. 45 (4) (2011) 1865–1871.
[31] P.Z. Culfaz, M. Haddad, M. Wessling, R. Lammertink, Fouling behavior of microstructured hollow fibers in cross-flow filtrations: critical flux determination and direct visual observation of particle deposition, J. Memb. Sci. 372 (1–2) (2011) 210–218.
[32] K. Michielsen, J.S. Kole, Photonic band gaps in materials with triply periodic surfaces and related tubular structures, Phys. Rev. B 68 (2003) 115107.
[33] O. Al-Ketan, R.K.A. Al-Rub, R. Rowshan, Mechanical properties of a new type of architected interpenetrating phase composite materials, Adv. Mater. Technol. (2016) 1600235.
[34] O. Al-Ketan, M. Adel Assad, R.K. Abu Al-Rub, Mechanical properties of periodic interpenetrating phase composites with novel architected microstructures, Compos. Struct. 176 (2017) 9–19.
[35] T. Femmer, A.J. Kuehne, M. Wessling, Estimation of the structure dependent performance of 3-D rapid prototyped membranes, Chem. Eng. J. 273 (2015) 438–445.
[36] M. Saeed, M.-H. Kim, Thermal and hydraulic performance of SCO2 PCHE with different fin configurations, Appl. Therm. Eng. 127 (2017) 975–985.
[37] C.J. Geankoplis, Transport processes and separation process principles, fourth ed., 2003, p. 475.
[38] J. Tian, T. Kim, T.J. Lu, H.P. Honson, D.T. Queheillalt, D.J. Sypeck, H.N.G. Wadley, The effects of topology upon fluid-flow and heat-transfer within cellular copper structures, Int. J. Heat Mass Transf. 47 (14) (2004) 3171–3186.